Applied Catalysis B: Environmental 227 (2018) 340–348

Contents lists available at ScienceDirect

Applied Catalysis B: Environmental

journal homepage: www.elsevier.com/locate/apcatb

Promotion of electrochemical oxygen evolution reaction by chemical coupling of cobalt to molybdenum carbide

MinJoong Kim[a], Sunghyun Kim[b], DongHoon Song[a], SeKwon Oh[a], Kee Joo Chang[b], EunAe Cho[a,*]

[a] Department of Materials Science and Engineering, Korea Advanced Institute of Science and Technology (KAIST), 291 Daehak-ro, Yuseong-gu, Daejeon, 34141, Republic of Korea

[b] Department of Physics, Korea Advanced Institute of Science and Technology (KAIST), 291 Daehak-ro, Yuseong-gu, Daejeon, 34141, Republic of Korea

ARTICLE INFO

Keywords:
Cobalt
Molybdenum carbide
Oxygen evolution reaction
Electrocatalyst
Chemical coupling

ABSTRACT

Herein, we report a novel strategy to promote electrochemical oxygen evolution reaction (OER) on cobalt (Co) surface by coupling Co to molybdenum carbide (Mo_2C). Chemically coupled Co and Mo_2C nanoparticles were synthesized through a simple heat treatment of the mixture containing Co and Mo precursors and graphitic carbon nitride (g-C_3N_4). Transmission electron microscopy (TEM) images obviously showed that Co and Mo_2C nanoparticles were coupled at Co/Mo_2C interfaces. X-ray photoelectron spectroscopy (XPS) and density functional theory (DFT) calculation results revealed that electrons were transferred from Co to Mo_2C nanoparticles across the interfaces. The electron transfer makes the Co surface more electrophilic by *d*-band center of Co upshift, leading to an increase in OH^- affinity. As a result, the Co nanoparticles coupled with Mo_2C have OER-favorable Co-oxo and Co-hydroxo configuration within their oxidized surfaces, and hence, can accelerate the overall OER than bare Co nanoparticles. This work demonstrates that the Co nanoparticles chemically coupled to Mo_2C exhibited excellent OER activity and stability in an alkaline electrolyte and suggests a promising way to design an active OER catalyst.

1. Introduction

Electrolyzing water into hydrogen and oxygen is an environmentally friendly method to store renewable energy in the form of hydrogen gas. The overall reaction of water electrolysis is divided into two half reactions: hydrogen evolution reaction (HER) at the cathode and oxygen evolution reaction (OER) at the anode. The efficiency of water electrolysis is primarily limited by a high anode overpotential due to sluggish kinetics of OER [1,2]. To facilitate the OER kinetics, RuO_2 and IrO_2 have been typically used as catalysts [3–6]. Although the scarcity and high cost of these noble-metal-based catalysts are impeding practical applications of water electrolysis, there is few viable alternatives with adequate stability under high anodic potentials in acidic electrolytes [7]. However, alkaline electrolytes allow a wider variety of OER catalyst materials including earth-abundant substances [8]. Therefore, it has been a major challenge to develop non-noble OER catalysts with high catalytic performances for alkaline water electrolysis [9].

A series of catalysts based on metallic cobalt (Co) or Co-oxides have been of interest owing to their low OER overpotentials in alkaline electrolytes [10]. Since OER occurs at high electrode potentials (E_o O_2/OH^- = 1.23 V_{RHE}), surface of the Co-based catalysts is oxidized by OH^- in alkaline electrolytes prior to occurrence of OER [11]. Among the oxidized phases of Co and Co-oxides, Co-(oxy)hydroxide (CoOOH) is known to be thermodynamically stable under general alkaline OER conditions [12,13]. According to the previous studies, the layered structure of CoOOH with edge-sharing of [CoO_6] subunits drives fast OER kinetics [14–21] and the Co cations coordinated by O (oxo) and OH (hydroxo) species (denoted as 'CoOOH configuration') serve as active sites to initiate and proceed OER [22]. However, in general, instead of the thermodynamically stable and highly OER-active CoOOH, kinetically-accessible hydrous oxide layers ($CoO_a(OH)_b(OH_2)_c$) are formed *in-situ* on the surface of Co and Co-oxides during OER [22]. In the hydrous oxide layers, Co cations have a variety of oxo and hydroxo configurations different from the CoOOH configuration. Thus, to enhance OER activity of Co-based catalysts, it is required to form CoOOH-like configuration in their surface hydrous oxide layers [23–25]. However, since the surface layers develop *in-situ*, it is a challenge to control the Co-oxo and Co-hydoxo configurations in the surface hydrous oxide layers toward the CoOOH configuration.

Recently, Co chalcogenides incorporated with a non-metal element, such as a selenide ($CoSe_2$) [26,27], phosphide (CoP) [28–30], nitride

* Corresponding author.
E-mail address: eacho@kaist.ac.kr (E. Cho).

https://doi.org/10.1016/j.apcatb.2018.01.051
Received 16 October 2017; Received in revised form 19 January 2018; Accepted 22 January 2018
0926-3373/ © 2018 Elsevier B.V. All rights reserved.

(Co_4N) [31] and boride (Co_2B) [32], have been reported to have OER activities comparable with RuO_2 and IrO_2. Due to the differences in the physical and chemical properties, those non-metal elements change the electronic structure of Co [28,32]. The changes in the electronic structure of Co surface facilitates the formation of hydrous oxide layers containing Co-oxo and Co-hydroxo species with Co^{3+}-OH and Co^{4+}-O [28]. As a result, Co-chalcogenides form an effective core-shell like structure composed of OER-active surface layer and electrically-conductive chalcogenide core. As a similar approach to modulate the electronic structure of surface Co, Mn_3O_4-supported $CoSe_2$ [33], Co-oxides@Au core-shell structures [34] and Co-oxides with nitrogen-doped carbon [35–38] have been proposed. In those studies, interatomic interactions between the Co-selenide or Co-oxides and other materials also enhanced OER activity of the Co-selenide or Co-oxides by modulating the electronic structure of the surface Co [34,39]. Those results demonstrate that interatomic coupling of Co to other elements or compounds can be an effective way to change surface electronic structure of Co and thereby improve OER activity.

Herein, we report a novel strategy to develop efficient OER catalysts. Our key idea was to form OER-active hydrous oxide layers on the surface of metallic Co nanoparticles by modulating electronic structure of Co. In the metallic Co-based core and hydrous oxide shell structure, metallic Co would be more favorable for OER rather than the previously reported chalcogenide or oxide-based Co compounds owing to the higher electrical conductivity. To modulate electronic structure of Co, Co nanoparticles were chemically coupled to molybdenum carbide (Mo_2C) nanoparticles. Transition metal carbides have affected electrocatalytic property of an admetal by changing electronic structure of the admetal surface [40]. Among various transition metal carbides, Mo_2C was employed in this study since Co-Mo coupling exhibited beneficial effects on oxygen electrocatalysis of Co [41,42]. Although Mo_2C is known to be unstable under the high OER overpotential [43], it was expected that Mo_2C could affect formation of the surface hydrous oxide layers prior to the occurrence of OER. The chemically coupled Co and Mo_2C nanoparticles were synthesized through a simple heat treatment of a Co and Mo precursor mixture with the addition of graphitic carbon nitride (g-C_3N_4) as a carbon source. Co nanoparticles coupled with Mo_2C nanoparticles were effectively oxidized to form the surface hydrous oxide layers with excellent OER activity. The effects of chemical coupling of Co to Mo_2C on the surface property and OER kinetics of Co were investigated through extensive characterization methods in combination with density functional theory (DFT) calculations.

2. Experimental

2.1. Material synthesis

Graphitic carbon nitride (g-C_3N_4) was used as a carbon source for the carburizing reaction of Mo into Mo_2C. To prepare g-C_3N_4, dicyandiamide ($C_2H_4N_4$) was heat treated at 550 °C for 4 h under an Ar gas atmosphere. After the heat treatment, white-colored dicyandiamide was successfully transformed to yellow-colored g-C_3N_4 (Fig. A.1).

Chemically coupled Co and Mo_2C nanoparticles were synthesized from a heat treatment of the precursor mixture containing cobalt(II) acetate tetrahydrate ($(CH_3COO)_2Co{\cdot}4H_2O$), ammonium molybdate ($(NH_4)_2MoO_4$) and the synthesized g-$C_3N_4$ at 800 °C for 1 h under an Ar gas atmosphere. Co nanoparticles were synthesized using the same heat treatment conditions with the precursor mixture containing $(CH_3COO)_2Co{\cdot}4H_2O$ and g-C_3N_4 without $(NH_4)_2MoO_4$. Mo_2C nanoparticles were synthesized from a heat treatment of $(NH_4)_2MoO_4$ at 800 °C for 1 h under H_2/CH_4 (80/20 vol.%) gas. Heating rate was 5 °C min^{-1} for all the samples.

2.2. Physical characterization

The morphologies of the prepared samples were examined by scanning electron microscopy (SEM) and transmission electron microscopy (TEM). Phase analysis was performed using X-ray diffraction (XRD). The chemical states of the prepared samples were analyzed using X-ray photoelectron spectroscopy (XPS). XPS results were calibrated by using 284.8 eV of C—C bond as a reference. The composition of each metallic element (Co, Mo) and non-metallic element (C, N) was measured by using inductively coupled plasma-atomic emission spectroscopy (ICP-AES) and elemental analysis (EA), respectively. For ammonia-temperature programmed desorption (NH_3-TPD) analysis, all samples were preheated at 300 °C for 1 h under vacuum to clean the surface, and then, NH_3 was chemisorbed at 100 °C for 1 h. The chemisorbed NH_3 was desorbed by increasing the temperature to 900 °C, and a thermal conductivity detector (TCD) detected the desorbed NH_3. The Brunauer-Emmett-Teller (BET) surface area was measured after pretreatment at 200 °C for 1 h under vacuum.

2.3. Electrochemical analysis

All the electrochemical measurements were conducted in a standard three-compartment electrochemical cell using a glassy carbon electrode (GCE) in the form of a rotating disc electrode (RDE), Pt mesh and mercury/mercury oxide (Hg/HgO) electrode filled with 0.1 M sodium hydroxide (NaOH) solution, as the working, counter and reference electrodes, respectively. Deionized (DI) water was purified to remove iron (Fe) impurities that Fe content in the DI water was about 0.035 ppb. All potentials were measured at 20 °C in a 0.1 M potassium hydroxide (KOH) solution and referenced against the reversible hydrogen electrode (RHE). The potential difference between the Hg/HgO electrode and the RHE was obtained from a cyclic voltammetry (CV) curve measured in the hydrogen-saturated 0.1 M KOH solution using a Pt disc as the working electrode. The sweep rate was 0.1 mV s^{-1}. A catalyst ink slurry was prepared by mixing the catalysts with 2 mL of DI water and 100 μL of 5 wt.% Nafion solution as a binding material. After mixing and ultrasonication, a drop of the ink slurry was loaded onto the GCE substrate. The dried electrode was then transferred to the electrochemical cell. Catalyst loading on the GCE was 0.24 mg cm^{-2} for all samples. The RDE rotation rate was 1600 rpm, and the sweep rate was 5 mV s^{-1} during the OER measurements. For an accelerated stress test (AST), 2000 potential cycles were conducted from 1.3 to 1.7 V_{RHE} in an Ar-purged 0.1 M KOH solution at a scan rate of 0.1 V s^{-1}. Potential of zero charge (PZC) was examined in 2 mM sodium fluoride (NaF) solution with a 100 mHz frequency and a 10 mV potential amplitude after three OER cycles in 0.1 M KOH solution.

2.4. Computational calculations

We performed first-principles calculations within the framework of density functional theory (DFT) that employed the generalized gradient approximation of Perdew, Burke, and Ernzerhof (PBE) [44] for the exchange-correlation potential and the projected augmented wave (PAW) pseudopotentials [45], as implemented in the VASP code [46]. In addition, the effective on-site Coulomb repulsion U = 3.5 eV on the Co-3d orbitals was included. We adopted a (111)-oriented Co on a Mo_2C (110) substrate to reduce the strain on the Co. The wave functions were expanded in plane waves up to an energy cutoff of 400 eV, and a Monkhorst-Pack mesh [47] of 9 × 6 × 1 was used for Brillouin zone integration

3. Results and discussion

3.1. Material synthesis and characterization

Chemically coupled Co and Mo_2C nanoparticles were synthesized through a simple heat treatment of the precursor mixture containing cobalt and molybdenum precursors, and g-C_3N_4 (made from dicyandiamide, Fig. A.1). g-C_3N_4 was used as a carbon source for the

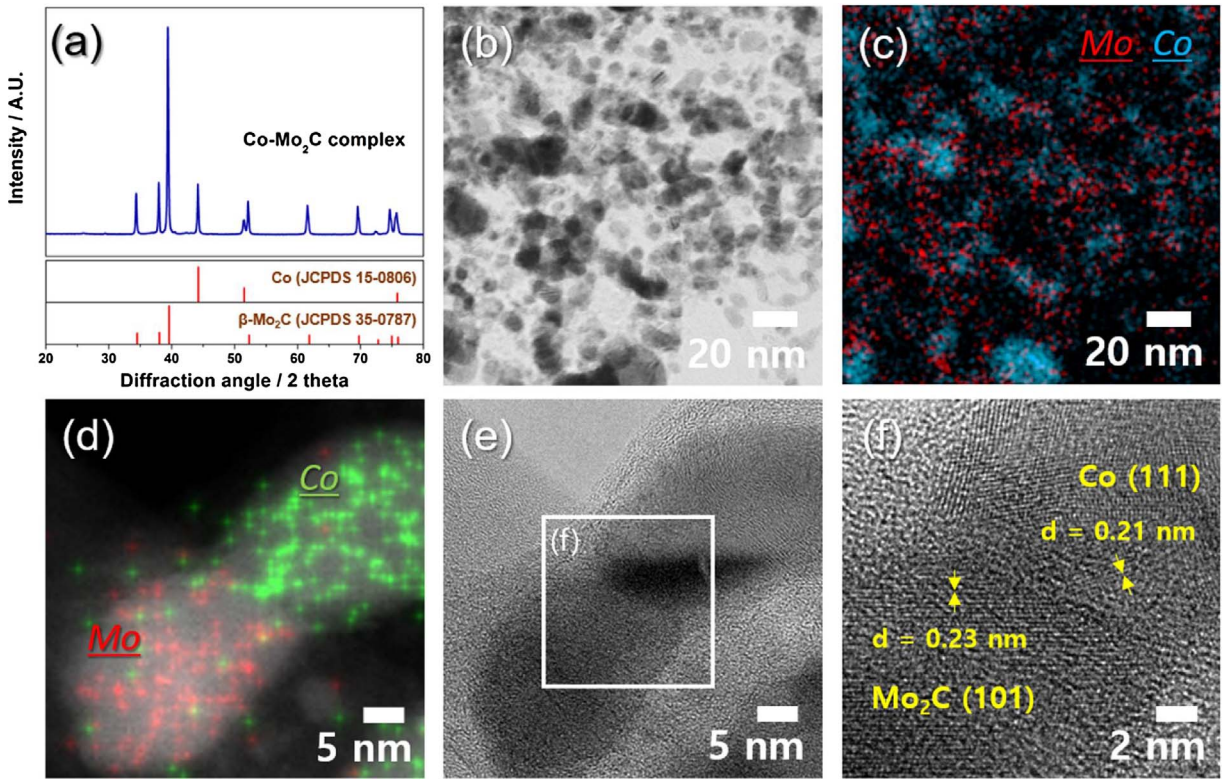

Fig. 1. (a) XRD pattern, (b), (e), (f) TEM images and (c), (d) TEM-EDS mapping images of the Co-Mo_2C NPs.

carburizing reaction of Mo into Mo_2C. XRD patterns in Fig. 1a show that crystalline Co (JCPDS 15-0806) and Mo_2C (β-Mo_2C; JCPDS 35-0787) phases were formed through the one-step heat treatment. To make crystalline Co and Mo_2C, the heat treatment was conducted at 800 °C for 1 h under an Ar gas atmosphere (Fig. A.2). The Co and Mo contents measured by ICP-AES were 30.1 and 55.3 wt.%, respectively.

For comparison, each of Co and Mo_2C samples was prepared. The Co sample was synthesized through the same process without the Mo precursor in the precursor mixture, and crystalline Co (JCPDS 15-0806) was obtained (Fig. A.3). On the other hand, using the same process without the Co precursor in the precursor mixture, MoO_2 and Mo were produced instead of Mo_2C. Only if a sufficient amount of cobalt precursor was added to the precursor mixture, MoO_2 and Mo were completely converted to Mo_2C, and Co was inevitably present in the product (Fig. A.4). These results demonstrate that Co is essential in the carburization reaction of Mo by anchoring carbon gas generated from the decomposition of g-C_3N_4. A previous study also suggested that a transition metal (Fe) facilitated carbide formation of a refractory metal (W) by anchoring the carbon [48]. For this reason, the Mo_2C sample was synthesized through a heat treatment of the Mo precursor at 800 °C for 1 h under H_2/CH_4 (80/20 vol.%) gas, and crystalline β-Mo_2C (JCPDS 35-0787) was obtained (Fig. A3).

TEM images (Fig. 1b and Fig. A.5a) show that the prepared Co-Mo_2C sample was composed of nanoparticles with sizes of ~20–30 nm (denoted as 'Co-Mo_2C NPs'). Carbon residues formed by the decomposition of g-C_3N_4 during the heat treatment at the high temperature [29,49] were observed in the TEM images. A SEM image (Fig. A.5b) shows that those nanoparticles agglomerated to form clusters with a size of ~200 nm with many open spaces. Owing to this porous structure, the Co-Mo_2C NPs had a high BET surface area of 143.0 $m^2 g^{-1}$. Similarly, the prepared Co sample was composed of Co nanoparticles with sizes of ~20–30 nm with carbon residue and a high BET surface area of 153.2 $m^2 g^{-1}$ (denoted as 'Co NPs') (Fig. A.5c and d). In both the Co-Mo_2C NPs and Co NPs, carbon residue was doped with small amount of nitrogen contained in g-C_3N_4. Nitrogen content in the carbon residue was measured to be about 0.8 and 1.4 at.% for the Co-Mo_2C NPs and Co NPs, respectively, from EA analysis. On the other hand, the prepared Mo_2C sample was composed of Mo_2C nanoparticles with sizes of ~200 nm and a low BET surface area of 7.3 $m^2 g^{-1}$ (denoted as 'Mo_2C NPs') (Fig. A.5e and f). Because the Mo_2C NPs were synthesized from a heat treatment under H_2/CH_4 (80/20 vol.%) gas without g-C_3N_4, the Mo_2C nanoparticles grew larger in size more than both the Co-Mo_2C NPs and the Co NPs synthesized from the precursor mixtures containing g-C_3N_4. The g-C_3N_4 could have served as a sacrificing template for the highly porous structure by prohibiting the growth and agglomeration of the primary nanoparticles during the heat treatment [50].

TEM energy dispersive spectroscopy (EDS) analysis of the Co-Mo_2C NPs demonstrated that the elemental mappings of Co and Mo rarely overlapped and were confined in each nanoparticle area (Fig. 1c and d). These results imply that the Co and Mo_2C nanoparticles formed separately, which is in good agreement with the XRD results that show formation of distinct phases of Co and Mo_2C. It should be noted that the Co and Mo_2C nanoparticles formed interfaces between the Co and Mo_2C phases (Fig. 1c–f). The d-spacing of each phase corresponds to the (111) plane of Co and the (101) plane of β-Mo_2C. As described above, Co played a key role in the synthesis of Mo_2C by enabling the carburization of neighboring Mo, which led to the formation of Mo_2C nanoparticles adjacent to the Co nanoparticles, generating interfaces between the Co and Mo_2C nanoparticles.

The chemical states of the Co-Mo_2C NPs were investigated using XPS. Core-level spectra of the metallic components in the Co-Mo_2C NPs (Co 2p and Mo 3d) were measured in comparison to those of the Co NPs and Mo_2C NPs. Fig. 2a shows that the Co-Mo_2C NPs and Co NPs have major Co $2p_{3/2}$ and Co $2p_{1/2}$ peaks for metallic Co (Co^0) and an oxidized Co surface. For the Co NPs, the Co $2p_{3/2}$ binding energy values were 778.2 and 779.7 eV. Considering that the reported binding energy values for Co^0 and Co_3O_4 are 778.1 (Co^0) and 779.6 eV (Co_3O_4), respectively [51], the Co NPs have almost ideal characteristics of Co^0 and oxidized surfaces (Co_3O_4). However, the Co $2p_{3/2}$ binding energy values of the Co-Mo_2C NPs were 778.5 (Co^0) and 780.3 eV (Co_3O_4), which are

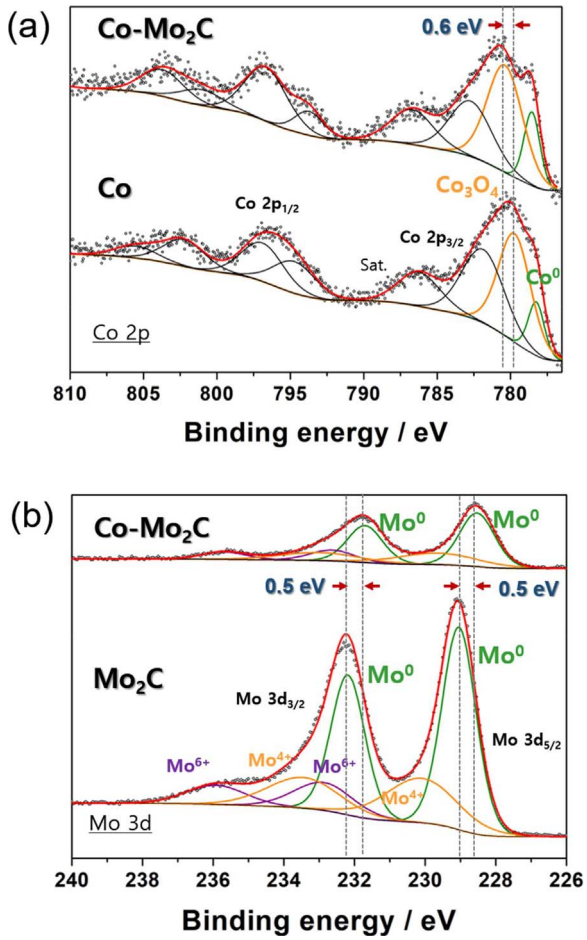

Fig. 2. (a) Co 2p spectra of the Co-Mo_2C NPs and Co NPs. (b) Mo 3d spectra of the Co-Mo_2C NPs and Mo_2C NPs.

Table 1
Co $2p_{2/3}$ and Mo $3d_{5/2}$ peaks of the Co NPs, Co-Mo_2C NPs and Mo_2C NPs before OER.

Sample	Co $2p_{2/3}$			Mo $3d_{5/2}$		
	1st peak	2nd peak	3rd peak	1st peak	2nd peak	3rd peak
Co	778.2 eV	779.7 eV	782.0 eV	–	–	–
Co-Mo_2C	778.5 eV	780.3 eV	782.9 eV	228.5 eV	229.5 eV	232.8 eV
Mo_2C	–	–	–	229.0 eV	229.8 eV	233.1 eV

positively shifted from those of the Co NPs by 0.3 and 0.6 eV, respectively. Chemical shifts in the core-level binding energy were also observed in the Mo 3d spectrum of the Co-Mo_2C NPs compared with that of the Mo_2C NPs. As shown in Fig. 2b, the Co-Mo_2C NPs and the Mo_2C NPs exhibited major peaks for elemental Mo^0 (Mo_2C) and minor peaks for Mo^{4+} and Mo^{6+} (surface oxides), similar to the previous results [52,53]. The Mo_2C NPs exhibited Mo $3d_{5/2}$ and Mo $3d_{3/2}$ peaks for elemental Mo (Mo^0) at 229.0 and 232.2 eV, respectively. However, the Co-Mo_2C NPs showed Mo $3d_{5/2}$ and Mo $3d_{3/2}$ peaks for Mo^0 at 228.5 and 231.7 eV, respectively, which were negatively shifted by 0.5 eV from those of the Mo_2C NPs. The minor peaks for Mo^{4+} and Mo^{6+} also negatively shifted by about 0.3 eV. In other words, for the Co-Mo_2C NPs, the Co 2p and Mo 3d spectra exhibited binding energy shifts of 0.3–0.6 eV, but in opposite direction, from their original values in the Co NPs and Mo_2C NPs as summarized in Table 1. It has been reported that core-level shift in chemically coupled elements, such as bulk alloys or adlayers on a substrate, are largely affected by interatomic charge transfers between the coupled elements [54,55]. A decrease of valence-electron charge leads to an increase in binding energy, whereas an increase of valence-electron charge leads to a decrease in binding energy [55]. Therefore, the binding energy shifts of the Co 2p and Mo 3d spectra in the opposite direction, can be attributed to the transfer of valence electrons from Co to Mo_2C across their interfaces. The interatomic charge transfer and the resulting modulation of the surface electronic structure can have strong effects on the catalytic performance of the Co nanoparticles, as demonstrated below.

3.2. Electrochemical oxygen evolution reaction activity

The catalytic performance of the Co-Mo_2C NPs for OER was investigated using a standard three-electrode cell and was compared with the Co NPs, Mo_2C NPs and commercially purchased RuO_2. The catalyst loading on a GCE was 0.24 mg cm^{-2}. Fig. 3a shows the IR-corrected OER polarization curves measured in 0.1 M KOH solution. The Co-Mo_2C NPs exhibited higher OER current density than the Co NPs and Mo_2C NPs over the entire potential area. RuO_2 exhibited a lower on-set potential for OER than the Co-Mo_2C NPs. However, with increasing current density, the overpotential of RuO_2 increased rapidly. As a measure of OER activity, the overpotential at 10 mA cm^{-2} is generally used [32]. As presented in Fig. 3b, the Co-Mo_2C NPs had a much lower overpotential (347 mV) than the Co NPs (377 mV), Mo_2C NPs (not available) and even RuO_2 (370 mV) at 10 mA cm^{-2}. Mo_2C seems to be almost inactive for OER. The corresponding Tafel slope was estimated to be 38 mv dec^{-1} for the Co-Mo_2C NPs, which was still lower than those for the Co NPs (48 mV dec^{-1}) and even RuO_2 (65 mV dec^{-1}), as shown in Fig. 3c. Nyquist plots measured at 1.6 V_{RHE} support the results observed from the OER polarization curves and Tafel slopes. The Co-Mo_2C NPs exhibited the smallest semi-circle, indicating the lowest charge-transfer resistance (Fig. 3d). The low Tafel slope and charge-transfer resistance of the Co-Mo_2C NPs indicates that the high OER activity is ascribed to enhanced kinetic properties.

The Faradic efficiency for OER on the Co-Mo_2C NPs was compared against that of RuO_2 using a rotating ring-disc experiment (RRDE). The Co-Mo_2C NPs and RuO_2 catalysts were loaded onto a glassy carbon disc, and 200 μA of anodic current was applied to the catalyst-loaded disc for OER. At the same time, 0.4 V_{RHE} was applied to the adjacent Pt ring for the reduction of the evolved oxygen. As shown in Fig. 3e, the measured ring currents of the Co-Mo_2C NPs and RuO_2 were almost the same during the oxygen evolving conditions at an anodic current of 200 μA. These results imply that the Faradic efficiency for OER on the Co-Mo_2C NPs is similar to that of the noble-metal-based RuO_2. The electrochemical durability of the Co-Mo_2C NPs under OER conditions was evaluated by cycling the potential from 1.3 to 1.7 V_{RHE} at a scan rate of 0.1 V s^{-1}. Over 2000 cycles, the overpotential at 10 mA cm^{-2} for the Co-Mo_2C NPs increased by only 8 mV (Fig. 3f), whereas that of RuO_2 increased by 42 mV (Fig. A.6). In summary, the Co-Mo_2C NPs synthesized in this study exhibits excellent OER activity and durability and is superior to RuO_2. In terms of the overpotential at 10 mA cm^{-2}, the OER activity of the Co-Mo_2C NPs synthesized in this study is comparable to the best Co-based OER catalysts reported to date, as summarized in Table A.2.

It is interesting that the Co-Mo_2C NPs exhibited a higher OER activity than the Co NPs despite less loading of active Co on the GCE for the OER tests (loading on GCE was 0.24 mg cm^{-2} for the Co-Mo_2C NPs and Co NPs). Since Mo_2C was inactive to OER as shown in Fig. 3a and nitrogen-doped carbon is generally known to be inactive, the enhanced OER activity of the Co-Mo_2C NPs over the Co NPs can be attributed to the enhanced OER capability of the Co nanoparticles in Co-Mo_2C NPs. As a parameter to determine the OER capability of the surface Co cation sites, the turnover frequency (TOF) for OER at $\eta = 350$ mV was calculated for 1) total number of moles of Co cations loaded on the GCE and 2) number of active surface Co cations from electrochemical surface area (ECSA). ECSA was calculated from the charge of the oxidation reaction from Co^{2+} to Co^{3+} prior to OER (Fig. A.7). As summarized in Table 2, the TOFs of the Co-Mo_2C NPs were about 5-times higher than

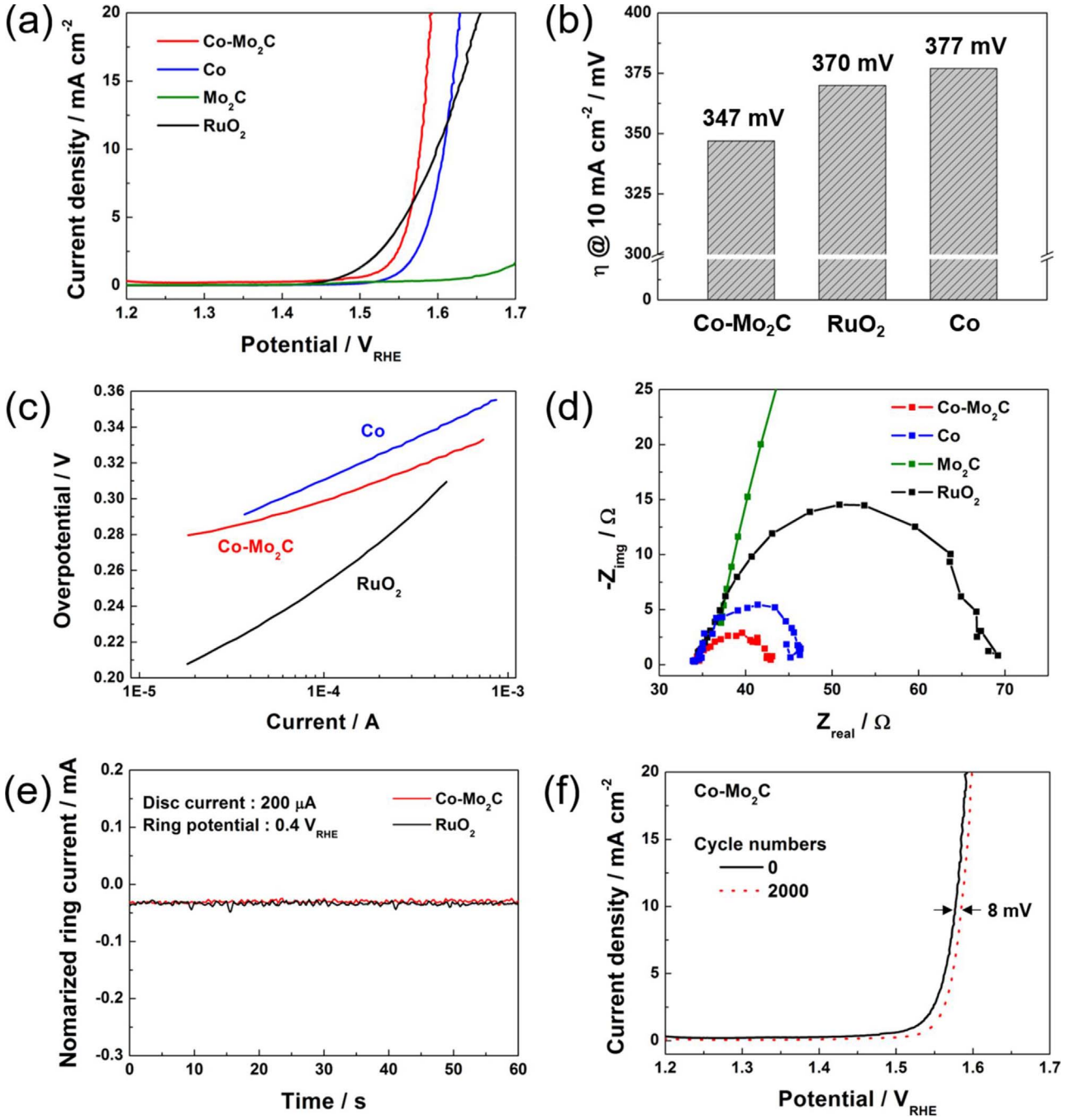

Fig. 3. (a) IR-corrected OER polarization curves, (b) overpotentials at 10 mA cm^{-2}, (c) Tafel slopes, and (d) Nyquist plots of the Co-Mo_2C NPs, Co NPs, Mo_2C NPs, and commercial RuO_2 measured in 0.1 M KOH solution. (e) Ring currents of the Co-Mo_2C NPs and commercial RuO_2 at a disc current of 200 μA and a ring potential of 0.4 V_{RHE}. (f) OER polarization curves of the Co-Mo_2C NPs before and after 2000 potential cycles from 1.3 to 1.7 V_{RHE} at a scan rate of 0.1 V s^{-1} in 0.1 M KOH solution.

Table 2
TOFs of the Co NPs and Co-Mo_2C NPs at η = 350 mV.

	Co	Co-Mo_2C
TOF for total Co cations	0.0057 s^{-1}	0.0252 s^{-1}
TOF for surface Co cations	0.108 s^{-1}	0.515 s^{-1}

those of the Co NPs, reflecting that the Co nanoparticles in the Co-Mo_2C NPs had significantly enhanced OER capability per surface Co cation than that for the Co NPs. These results demonstrate that the Mo_2C nanoparticles in the Co-Mo_2C NPs have beneficial effects on the OER kinetics of the adjacent Co nanoparticles. With increasing or decreasing ratio of Co to Mo content in the precursor mixtures from 1, the OER activity of the synthesized samples decreased, reflecting that the chemical coupling of Co to Mo_2C with the optimal ratio significantly enhanced the OER capability of surface Co cations (Fig. A.8).

3.3. Effects of the chemical coupling of Co to Mo_2C on OER kinetics

Combining the experimental observations discussed thus far, the Co-Mo_2C NPs have excellent OER activity in alkaline electrolytes owing to the enhanced OER capability of the Co surface cations as a result of the chemical coupling of Co to the Mo_2C nanoparticles. As described in Introduction, metallic Co and Co-oxides form surface hydrous oxide layers of $CoO_a(OH)_b(OH_2)_c$ with various Co-oxo and Co-hydroxo

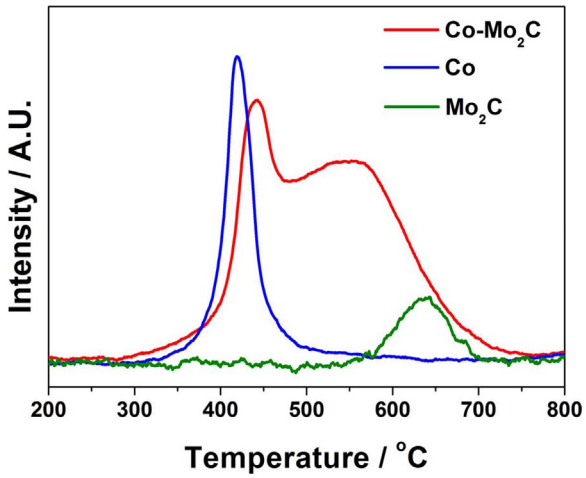

Fig. 4. NH_3-TPD results of the Co-Mo_2C NPs, Co NPs, and Mo_2C NPs.

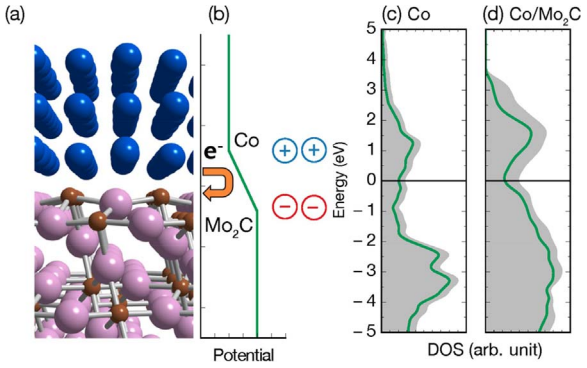

Fig. 5. (a) The atomic structure of Co/Mo_2C. Blue, pink, and brown balls represent Co, Mo, and C atoms, respectively. (b) A schematic diagram of the potential shift due to electron transfer across the interface. Total densities of states (gray shade) and the projected DOS of the *d*-orbitals of Co (green line) for (c) Co slab and (d) Co/Mo_2C. (For interpretation of the references to colour in this figure legend, the reader is referred to the web version of this article.)

configurations rather than the thermodynamic stable CoOOH [22]. The Co cations coordinated by oxo and hydroxo species in the outermost hydrous oxide layers serve as active site for OER. Therefore, it can be inferred that the interactions between Co and Mo_2C at their interfaces would enhance the OER capability of Co cations in the hydrous oxide layers.

The formation of hydrous oxide layers is initiated by OH^- adsorption and proceeds by reaction with the adsorbed OH^- [34]. OH^- is a species like building block to form hydrous oxide layers, so OH^- adsorption on the Co surface can determine structure of the hydrous oxide layers. In this study, all of the OER cycles were conducted in 0.1 M KOH at room temperature with the identical activity of OH^- (a_{OH^-}). Thus, it can be regarded that OH^- affinity of Co surface of each sample largely affected OH^- adsorption. OH^- is well known as a strong Lewis base, which chemically adsorbs on electrophilic (or Lewis acidic) surfaces by donating its lone-pair electrons of oxygen. Because NH_3 is also a strong Lewis base with a lone pair of electrons of nitrogen, NH_3-TPD method can be employed to indirectly evaluate OH^- affinity of the Co surface.

Fig. 4 presents the NH_3-TPD results of the Co-Mo_2C NPs, Co NPs and Mo_2C NPs measured after NH_3 chemisorption at 100 °C for 1 h. The Co NPs exhibited a sharp desorption peak at 421 °C and the Mo_2C NPs exhibited a broad desorption peak at approximately 635 °C. Interestingly, the Co-Mo_2C NPs exhibited a sharp desorption peak at a higher temperature (438 °C) than the Co NPs and a broad desorption peak at lower temperature (540 °C) than the Mo_2C NPs. These results indicate that the chemical coupling of Co and Mo_2C nanoparticles changed the electrophilic properties of each nanoparticle surface, Co surface more electrophilic and Mo_2C surface less electrophilic. Previous studies also reported that interatomic coupling of Co to other elements or compounds changes electrophilic property of Co surface [28,34].

This change in surface electrophilic property could be strongly associated with the electronic structure of metal surface. DFT calculations for the Co-Mo_2C model system showed that electrons were transferred from Co to Mo_2C across the interface (Fig. 5a and b), in a good agreement with the XPS results (Fig. 2). Due to the electron transfer, electronic structure of Co was changed that the *d*-band center of Co upshifted by approximately 0.25 eV with respect to the Fermi level when coupled with Mo_2C (Fig. 5c and d). The *d*-band center is useful to predict the adsorption behavior of small molecules on metal surface [56]. As the adsorption energies of small molecules on metal surface increase as a function of metal *d*-band center [56], it is known that adsorption of OH^- on metal surface would be strengthened by *d*-band center of metal upshift [57]. In this sense, the electron transfer induced *d*-band center upshift could make the Co surface more electrophilic to increase OH^- affinity. As mentioned above, OH^- is a core molecule to form hydrous oxide layers during OER, so it can be deduced that the increase in OH^- affinity on the Co surface largely affects the structural and chemical properties of hydrous oxide layers of the Co-Mo_2C NPs. To clarify the nature of hydrous oxide layers, we measured *ex-situ* XPS spectra of the Co-Mo_2C NPs and Co NPs after OER cycles.

Fig. 6 show *ex-situ* XPS Co 2p and O 1s spectra for the Co-Mo_2C NPs and the Co NPs after three OER cycles. As shown in Fig. 6a, both the Co-Mo_2C NPs and Co NPs exhibited more oxidized Co 2p peaks than Co^0 with a low satellite peak, corresponding to Co^{3+}. Contrary to Co 2p spectra, there was a remarkable difference in O 1s spectra; the Co-Mo_2C

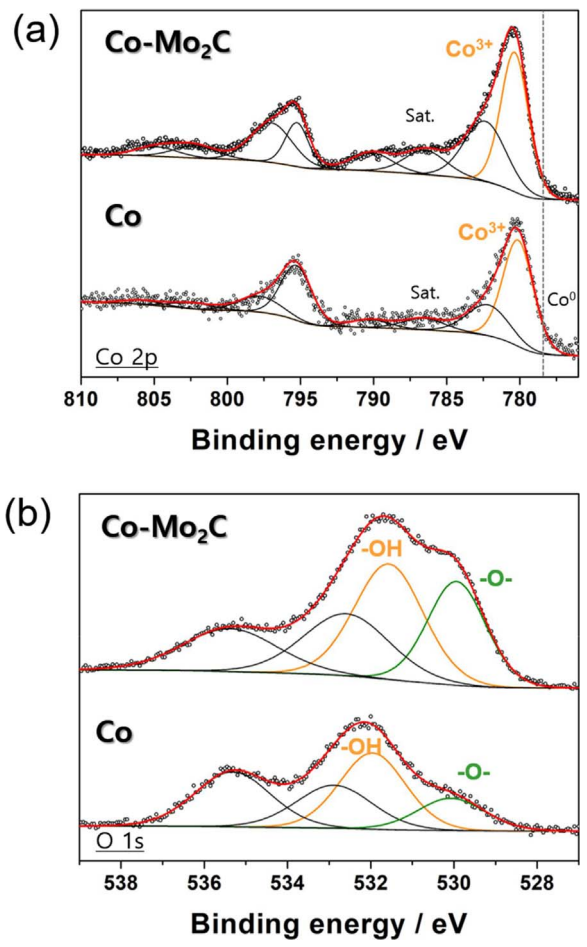

Fig. 6. (a) Co 2p and (b) O 1s spectra of the Co-Mo_2C NPs and Co NPs after three OER cycles.

Table 3
Co $2p_{2/3}$ and O 1 s peaks of the Co NPs and Co-Mo_2C NPs after 3 OER cycles.

Sample	Co $2p_{2/3}$		O 1s	
	1st peak	2nd peak	1st peak	2nd peak
Co	780.2 eV	782.4 eV	530.0 eV	531.9 eV
Co-Mo_2C	780.4 eV	782.6 eV	530.0 eV	531.6 eV

NPs had higher proportion of oxo (–O–) species than the Co NPs as shown in Fig. 6b. The detailed XPS fitting data is summarized in Table 3. It seems that more electrophilic Co surface of the Co-Mo_2C NPs could attract OH^- more strongly than that of the Co NPs, which could lead to higher proportion of oxo coordinated-Co cations in the hydrous oxide layers of the Co-Mo_2C NPs. The higher proportion of oxo co-ordinated-Co cations like [CoO_x] resembles the structure of CoOOH configured by edge-sharing of [CoO_6] subunits. So, Co 2p and O 1s spectra of the Co-Mo_2C NPs were very similar to those of the previously reported CoOOH [58], whereas those of Co NPs were lack of oxo species in O 1s spectra. The similar XPS spectra means that the hydrous oxide layers of the Co-Mo_2C NPs could have subunits containing similar Co-oxo and Co-hydroxo configurations with CoOOH. It is known that the subunits of CoOOH are highly favorable for OER because OER-active Co^{3+}-OH and Co^{4+}-O moieties are likely formed within those subunits during OER [59,60]. Therefore, this *ex-situ* XPS study implies that the hydrous oxide layers of the Co-Mo_2C NPs would also have suitable Co-oxo and Co-hydroxo configuration to form the OER-active moieties during OER due to the configurational similarity with CoOOH. The surface oxo and hydroxo ratio of the Co-Mo_2C was little changed after 1000 potential cycles from 1.3 to 1.7 V_{RHE} as shown in Fig. A.9. This is the reason of the excellent electrochemical stability of the Co-Mo_2C (Fig. 3f). Even though this *ex-situ* measurement method cannot display real time transformation of Co surface to hydrous oxide layers, it clearly showed the difference in basic configurations of the hydrous oxides on the Co-Mo_2C NPs and Co NPs.

In case of Mo, most of the Mo_2C nanoparticles were dissolved into molybdate anion (MoO_4^{2-}) during the first OER cycle (Fig. A.10), because Mo is not stable in an alkaline solution [41]. However, there was negligible difference between the second and the third OER plots, reflecting that there was little dissolution of Mo into MoO_4^{2-} after the first OER cycle (Table A.1). The Faradaic efficiency calculated from the RRDE test (Fig. 3e) also supports that there was negligible effect of Mo dissolution on the measured OER currents. All those results demonstrate that although Mo is not stable under alkaline OER condition and most of the Mo_2C nanoparticles were dissolved during the first OER cycle, Mo_2C contributed to formation of hydrous oxide layers with CoOOH-like configuration on the coupled Co surfaces and to enhancement of OER activity. In addition, OER activity of Co NPs was not affected by MoO_4^{2-} ions in 0.1 M KOH solution (Fig. A. 11), implying that MoO_4^{2-} ions dissolved from the Co-Mo_2C NPs into the solution had little effects on the formation of hydrous oxides and subsequent OER on Co surface.

To more understand nature of the hydrous oxide layers on the Co-Mo_2C NPs and the Co NPs, PZC was measured. PZC is known to have a linear relationship with the electrochemical work function of the electrode in contact with the electrolyte [61]. Therefore, it is expected that the PZC measurement after OER provides information about electron transfer between the oxidized catalysts and the electrolyte. Fig. 7 presents the measured PZCs of the Co-Mo_2C NPs and Co NPs after three OER cycles. The Co-Mo_2C NPs exhibited a higher PZC than the Co NPs by 0.23 V. A higher PZC indicates a higher electrochemical work function, which means that the electron transfer from the electrode to the electrolyte becomes more difficult. In other words, a higher PZC means that the electrode is more favorable for oxidation reaction like OER by easily accepting electrons from reactants or intermediates. As

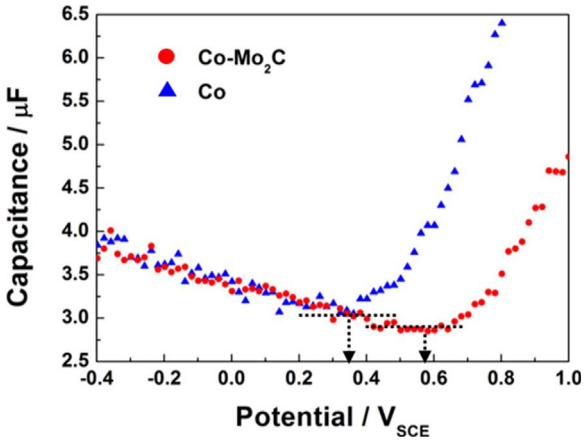

Fig. 7. PZCs of the Co-Mo_2C NPs and Co NPs measured in 2 mM NaF solution after three OER cycles.

the structure and composition of the Co NPs and Co-Mo_2C NPs changes during OER, water molecules and reaction intermediates for OER can be bonded in different ways for the Co NPs and Co-Mo_2C NPs [62], contributing to the different PZC values between the Co NPs and Co-Mo_2C NPs. The PZC results support that the hydrous oxide layers of the Co-Mo_2C NPs could be more active for OER than those of the Co NPs, and demonstrates that oxo and hydroxo configurations of Co cations in the hydroxide layers is a crucial factor for determining OER activity. By combining the *ex-situ* XPS and the PZC results after OER, it can be concluded that the excellent OER activity of the Co-Mo_2C NPs would be ascribed to the OER-favorable Co-oxo and Co-hydroxo configuration.

In summary, all the experimental and computational results demonstrate that the chemical coupling of Co to Mo_2C induces electron transfer from Co to Mo_2C across their interfaces, making Co surface more electrophilic by *d*-band center of Co upshift. Due to this change in the electronic structure of Co, the Co nanoparticles in the Co-Mo_2C NPs could be effectively oxidized to form active hydrous oxide layers for OER. Thus, Co nanoparticles in the Co-Mo_2C NPs exhibited excellent OER activity and stability in alkaline electrolyte.

4. Conclusion

We synthesized a chemically coupled Co and Mo_2C nanoparticles using a simple heat treatment to promote OER on Co surface. The Co-Mo_2C NPs had highly porous structure composed of ~20-30 nm-sized nanoparticles. Chemical coupling at the interface between Co and Mo_2C nanoparticles induced electron transfer from Co to Mo_2C, as demonstrated from binding energy shift in XPS spectra. NH_3-TPD results showed that Co surface coupled with Mo_2C was more electrophilic with high OH^- affinity than bare Co surface. DFT calculation revealed that the electron transfer from Co to Mo_2C makes *d*-band center of Co upshift, which induced increase in OH^- affinity on Co surface. The more electrophilic Co surface with high OH^- affinity could lead to formation of surface hydrous oxide layers with higher proportion of oxo-coordinated Co cations. And, the hydrous oxide layers of the Co-Mo_2C NPs exhibited the higher electrochemical work function than those of the Co NPs. The higher electrochemical work function imply that the surface hydrous oxide layers of the Co-Mo_2C NPs are more advantageous to facilitate OER, which is ascribed to the OER favorable Co-oxo and Co-hydroxo configuration resembling CoOOH. Therefore, the Co nanoparticles chemically coupled to Mo_2C nanoparticles exhibited superior OER activity than Co and even RuO_2 in alkaline electrolytes. This study provides a novel and practical method to design a new class of promising materials for OER in alkaline electrolysis through fundamental investigation.

Acknowledgements

This work was supported by the Korea Evaluation Institute of Industrial Technology (KEIT) (Grant No. 10052823), and the Korea Institute of Energy Technology Evaluation and Planning (KETEP) (Grant No. 20153010041750) funded by the Ministry of Trade, Industry & Energy of Korea. This work was also supported by Samsung Science and Technology Foundation (Grant No. SSTF-BA1401-08).

Appendix A. Supplementary data

Supplementary data associated with this article can be found, in the online version, at https://doi.org/10.1016/j.apcatb.2018.01.051.

References

[1] H. Dau, C. Limberg, T. Reier, M. Risch, S. Roggan, P. Strasser, The mechanism of water oxidation: from electrolysis via homogeneous to biological catalysis, ChemCatChem 2 (2010) 724–761.
[2] S. Park, Y. Shao, J. Liu, Y. Wang, Oxygen electrocatalysts for water electrolyzers and reversible fuel cells: status and perspective, Energy Environ. Sci. 5 (2012) 9331–9344.
[3] S. Trasatti, Electrocatalysis in the anodic evolution of oxygen and chlorine, Electrochim. Acta 29 (1984) 1503–1512.
[4] J. Rossmeisl, Z.-W. Qu, H. Zhu, G.-J. Kroes, J.K. Nørskov, Electrolysis of water on oxide surfaces, J. Electroanal. Chem. 607 (2007) 83–89.
[5] Y. Lee, J. Suntivich, K.J. May, E.E. Perry, Y. Shao-Horn, Synthesis and activities of rutile IrO_2 and RuO_2 nanoparticles for oxygen evolution in acid and alkaline solutions, J. Phys. Chem. Lett. 3 (2012) 399–404.
[6] C.C.L. McCrory, S. Jung, J.C. Peters, T.F. Jaramillo, Benchmarking heterogeneous electrocatalysts for the oxygen evolution reaction, J. Am. Chem. Soc. 135 (2013) 16977–16987.
[7] C.C.L. McCrory, S. Jung, I.M. Ferrer, S.M. Chatman, J.C. Peters, T.F. Jaramillo, Benchmarking hydrogen evolving reaction and oxygen evolving reaction electrocatalysts for solar water splitting devices, J. Am. Chem. Soc. 137 (2015) 4347–4357.
[8] D.E. Hall, Alkaline water electrolysis anode materials, J. Electrochem. Soc. 132 (1985) 41C–48C.
[9] S. Marini, P. Salvi, P. Nelli, R. Pesenti, M. Villa, M. Berrettoni, G. Zangari, Y. Kiros, Advanced alkaline water electrolysis, Electrochim. Acta 82 (2012) 384–391.
[10] Y. Jiao, Y. Zheng, M. Jaroniec, S.Z. Qiao, Design of electrocatalysts for oxygen- and hydrogen-involving energy conversion reactions, Chem. Soc. Rev. 44 (2015) 2060–2086.
[11] R. Subbaraman, D. Tripkovic, K.-C. Chang, D. Strmcnik, A.P. Paulikas, P. Hirunsit, M. Chan, J. Greeley, V. Stamenkovic, N.M. Markovic, Trends in activity for the water electrolyser reactions on 3d M(Ni,Co,Fe,Mn) hydr(oxy)oxide catalysts, Nat. Mater. 11 (2012) 550–557.
[12] M. Bajdich, M. García-Mota, A. Vojvodic, J.K. Nørskov, A.T. Bell, Theoretical investigation of the activity of cobalt oxides for the electrochemical oxidation of water, J. Am. Chem. Soc. 135 (2013) 13521–13530.
[13] M.S. Burke, L.J. Enman, A.S. Batchellor, S. Zou, S.W. Boettcher, Oxygen evolution reaction electrocatalysis on transition metal oxides and (oxy)hydroxides: activity trends and design principles, Chem. Mater. 27 (2015) 7549–7558.
[14] L. Trotochaud, S.L. Young, J.K. Ranney, S.W. Boettcher, Nickel–iron oxyhydroxide oxygen-evolution electrocatalysts: the Role of intentional and incidental iron incorporation, J. Am. Chem. Soc. 136 (2014) 6744–6753.
[15] D. Friebel, M.W. Louie, M. Bajdich, K.E. Sanwald, Y. Cai, A.M. Wise, M.-J. Cheng, D. Sokaras, T.-C. Weng, R. Alonso-Mori, R.C. Davis, J.R. Bargar, J.K. Nørskov, A. Nilsson, A.T. Bell, Identification of highly active Fe sites in (Ni,Fe)OOH for electrocatalytic water splitting, J. Am. Chem. Soc. 137 (2015) 1305–1313.
[16] M. Gong, Y. Li, H. Wang, Y. Liang, J.Z. Wu, J. Zhou, J. Wang, T. Regier, F. Wei, H. Dai, An advanced Ni–Fe layered double hydroxide electrocatalyst for water oxidation, J. Am. Chem. Soc. 135 (2013) 8452–8455.
[17] H. Chen, L. Hu, M. Chen, Y. Yan, L. Wu, Nickel-cobalt layered double hydroxide nanosheets for high-performance supercapacitor electrode materials, Adv. Funct. Mater. 24 (2014) 934–942.
[18] N. Han, F. Zhao, Y. Li, Ultrathin nickel–iron layered double hydroxide nanosheets intercalated with molybdate anions for electrocatalytic water oxidation, J. Mater. Chem. A3 (2015) 16348–16353.
[19] H.-Y. Wang, Y.-Y. Hsu, R. Chen, T.-S. Chan, H.M. Chen, B. Liu, Ni $^{3+}$-induced formation of active NiOOH on the spinel Ni-Co oxide surface for efficient oxygen evolution reaction, Adv. Energy Mater. 5 (2015) 1500091.
[20] L.-Z. Huang, L. Fang, T. Hassenkam, K.N. Dalby, K.G. Scheckel, H.C.B. Hansen, A one-step delamination procedure to form single sheet iron(III)-(oxy)hydroxides, J. Mater. Chem. A 1 (2013) 13664–13671.
[21] J.-X. Feng, H. Xu, Y.-T. Dong, S.-H. Ye, Y.-X. Tong, G.-R. Li, FeOOH/Co/FeOOH hybrid nanotube arrays as high-performance electrocatalysts for the oxygen evolution reaction, Angew. Chem. Int. Ed. 55 (2016) 3694–3698.
[22] R.L. Doyle, I.J. Godwin, M.P. Brandon, M.E.G. Lyons, Redox and electrochemical water splitting catalytic properties of hydrated metal oxide modified electrodes, Phys. Chem. Chem. Phys. 15 (2013) 13737–13783.
[23] Y.J. Sa, K. Kwon, J.Y. Cheon, F. Kleitz, S.H. Joo, Ordered mesoporous Co_3O_4 spinels as stable bifunctional, noble metal-free oxygen electrocatalysts, J. Mater. Chem. A 1 (2013) 9992–10001.
[24] B. Seo, Y.J. Sa, J. Woo, K. Kwon, J. Park, T.J. Shin, H.Y. Jeong, S.H. Joo, Size-dependent activity trends combined with in situ X-ray absorption spectroscopy reveal insights into cobalt oxide/carbon nanotube-catalyzed bifunctional oxygen electrocatalysis, ACS Catal. 6 (2016) 4347–4355.
[25] H.-Y. Wang, S.-F. Hung, H.-Y. Chen, T.-S. Chan, H.M. Chen, B. Liu, In Operando identification of geometrical-site-dependent water oxidation activity of spinel Co_3O_4, J. Am. Chem. Soc. 138 (2016) 36–39.
[26] Q. Gao, X. Zhao, Y. Xiao, D. Zhao, M. Cao, A mild route to mesoporous Mo_2C–C hybrid nanospheres for high performance lithium-ion batteries, Nanoscale 6 (2014) 6151–6157.
[27] Y.-R. Zheng, M.-R. Gao, Q. Gao, H.-H. Li, J. Xu, Z.-Y. Wu, S.-H. Yu, An efficient CeO_2/$CoSe_2$ nanobelt composite for electrochemical water oxidation, Small 11 (2015) 182–188.
[28] Y.-P. Zhu, Y.-P. Liu, T.-Z. Ren, Z.-Y. Yuan, Self-supported cobalt phosphide mesoporous nanorod arrays: a flexible and bifunctional electrode for highly active electrocatalytic water reduction and oxidation, Adv. Funct. Mater. 25 (2015) 7337–7347.
[29] J. Ryu, N. Jung, J.H. Jang, H.-J. Kim, S.J. Yoo, In situ transformation of hydrogen-evolving CoP nanoparticles: toward efficient oxygen evolution catalysts bearing dispersed morphologies with Co-oxo/hydroxo molecular units, ACS Catal. 5 (2015) 4066–4074.
[30] S. Oh, H. Kim, Y. Kwon, M. Kim, E. Cho, H. Kwon, Porous Co–P foam as an efficient bifunctional electrocatalyst for hydrogen and oxygen evolution reactions, J. Mater. Chem. A4 (2016) 18272–18277.
[31] P. Chen, K. Xu, Z. Fang, Y. Tong, J. Wu, X. Lu, X. Peng, H. Ding, C. Wu, Y. Xie, Metallic Co_4N porous nanowire arrays activated by surface oxidation as electrocatalysts for the oxygen evolution reaction, Angew. Chem. Int. Ed. 54 (2015) 14710–14714.
[32] J. Masa, P. Weide, D. Peeters, I. Sinev, W. Xia, Z. Sun, C. Somsen, M. Muhler, W. Schuhmann, Amorphous cobalt boride (Co_2B) as a highly efficient nonprecious catalyst for electrochemical water splitting: oxygen and hydrogen evolution, Adv. Energy Mater. 6 (2016) 1502313.
[33] M.-R. Gao, Y.-F. Xu, J. Jiang, Y.-R. Zheng, S.-H. Yu, Water oxidation electrocatalyzed by an efficient Mn_3O_4/$CoSe_2$ nanocomposite, J. Am. Chem. Soc. 134 (2012) 2930–2933.
[34] B.S. Yeo, A.T. Bell, Enhanced activity of gold-supported cobalt oxide for the electrochemical evolution of oxygen, J. Am. Chem. Soc. 133 (2011) 5587–5593.
[35] T.Y. Ma, S. Dai, M. Jaroniec, S.Z. Qiao, Metal–organic framework derived hybrid Co_3O_4-carbon porous nanowire arrays as reversible oxygen evolution electrodes, J. Am. Chem. Soc. 136 (2014) 13925–13931.
[36] L. Wu, Q. Li, C.H. Wu, H. Zhu, A. Mendoza-Garcia, B. Shen, J. Guo, S. Sun, Stable cobalt nanoparticles and their monolayer array as an efficient electrocatalyst for oxygen evolution reaction, J. Am. Chem. Soc. 137 (2015) 7071–7074.
[37] H. Jin, J. Wang, D. Su, Z. Wei, Z. Pang, Y. Wang, In situ cobalt–cobalt oxide/N-doped carbon hybrids as superior bifunctional electrocatalysts for hydrogen and oxygen evolution, J. Am. Chem. Soc. 137 (2015) 2688–2694.
[38] Y. Zhao, B. Sun, X. Huang, H. Liu, D. Su, K. Sun, G. Wang, Porous graphene wrapped CoO nanoparticles for highly efficient oxygen evolution, J. Mater. Chem. A 3 (2015) 5402–5408.
[39] M.-R. Gao, X. Cao, Q. Gao, Y. Xu, Y. Zheng, J. Jiang, S. Yu, Nitrogen-doped graphene supported $CoSe_2$ nanobelt composite catalyst for efficient water oxidation, ACS Nano 8 (2014) 3970–3978.
[40] T.G. Kelly, J.G. Chen, Metal overlayer on metal carbide substrate: unique bimetallic properties for catalysis and electrocatalysis, Chem. Soc. Rev. 41 (2012) 8021–8034.
[41] B. Cao, G.M. Veith, R.E. Diaz, J. Liu, E.A. Stach, R.R. Adzic, P.G. Khalifah, Cobalt molybdenum oxynitrides: synthesis, structural characterization, and catalytic activity for the oxygen reduction reaction, Angew. Chem. Int. Ed. 52 (2013) 10753–10757.
[42] T. Sun, Q. Wu, R. Che, Y. Bu, Y. Jiang, Y. Li, L. Yang, X. Wang, Z. Hu, Alloyed Co–Mo nitride as high-performance electrocatalyst for oxygen reduction in acidic medium, ACS Catal. 5 (2015) 1857–1862.
[43] J.P. Perdew, K. Burke, M. Ernzerhof, Generalized gradient approximation made simple, Phys. Rev. Lett. 77 (1996) 3865–3868.
[44] M. Pourbaix, Atlas of Electrochemical Equilibria in Aqueous Solutions, second ed., National Association of Corrosion Engineers, Houston, 1974.
[45] P.E. Blöchl, Projector augmented-wave method, Phys. Rev. B 50 (1994) 17953–17979.
[46] G. Kresse, D. Joubert, From ultrasoft pseudopotentials to the projector augmented-wave method, Phys. Rev. B 59 (1999) 1758–1775.
[47] J.D. Pack, H.J. Monkhorst, Special points for brillouin-zone integrations, Phys. Rev. B 16 (1977) 1748–1749.
[48] Z. Yan, M. Cai, P.K. Shen, Nanosized tungsten carbide synthesized by a novel route at low temperature for high performance electrocatalysis, Sci. Rep. 3 (2013) 1646.
[49] M. Kim, D.-H. Nam, H.-Y. Park, C. Kwon, K. Eom, S. Yoo, J. Jang, H.-J. Kim, E. Cho, H. Kwon, Cobalt-carbon nanofibers as an efficient support-free catalyst for oxygen reduction reaction with a systematic study of active site formation, J. Mater. Chem. A 3 (2015) 14284–14290.
[50] N.S. Alhajri, D.H. Anjum, K. Takanabe, Molybdenum carbide–carbon nanocomposites synthesized from a reactive template for electrochemical hydrogen evolution, J. Mater. Chem. A.2 (2014) 10548.
[51] M.C. Biesinger, B.P. Payne, A.P. Grosvenor, L.W.M. Lau, A.R. Gerson, R.S.C. Smart, Resolving surface chemical states in XPS analysis of first row transition metals, oxides and hydroxides: Cr, Mn, Fe, Co and Ni, Appl. Surf. Sci. 257 (2011)

2717–2730.
[52] C. Wan, Y.N. Regmi, B.M. Leonard, Multiple phases of molybdenum carbide as electrocatalysts for the hydrogen evolution reaction, Angew. Chem. Int. Ed. 53 (2014) 6407–6410.
[53] W.-F. Chen, C.-H. Wang, K. Sasaki, N. Marinkovic, W. Xu, J.T. Muckerman, Y. Zhu, R.R. Adzic, Highly active and durable nanostructured molybdenum carbide electrocatalysts for hydrogen production, Energy Environ. Sci. 6 (2013) 943–951.
[54] M. Weinert, R.E. Watson, Core-level shifts in bulk alloys and surface adlayers, Phys. Rev. B 51 (1995) 17168–17180.
[55] J.A. Rodriguez, D.W. Goodman, The nature of the metal–metal bond in bimetallic surfaces, Science 257 (1992) 897–903.
[56] B. Hammer, J.K. Nørskov, Theoretical surface science and catalysis-calculations and concepts, Adv. Catal. 45 (2000) 71–129.
[57] S.T. Nguyen, H.M. Law, H.T. Nguyen, N. Kristian, S. Wang, S.H. Chan, X. Wang, Enhancement effect of Ag for Pd/C towards the ethanol electro-oxidation in alkaline media, Appl. Catal. B Environ. 91 (2009) 507–515.
[58] J. Yang, H. Liu, W.N. Martens, R.L. Frost, Synthesis and characterization of cobalt hydroxide cobalt oxyhydroxide, and cobalt oxide nanodiscs, J. Phys. Chem. C 114 (2010) 111–119.
[59] Y. Surendranath, M.W. Kanan, D.G. Nocera, Mechanistic studies of the oxygen evolution reaction by a cobalt-phosphate catalyst at neutral pH, J. Am. Chem. Soc. 132 (2010) 16501–16509.
[60] J.G. McAlpin, Y. Surendranath, M. Dinca, T.A. Stich, S.A. Stoian, W.H. Casey, D.G. Nocera, R.D. Britt, EPR. evidence for Co(IV) species produced during water oxidation at neutral pH, J. Am. Chem. Soc. 132 (2010) 6882–6883.
[61] C.H. Choi, H. Lim, M.W. Chung, J.C. Park, H. Shin, H. Kim, S.I. Woo, Long-range electron transfer over graphene-based catalyst for high-performing oxygen reduction reactions: importance of size, N-doping, and metallic impurities, J. Am. Chem. Soc. 136 (2014) 9070–9077.
[62] M. Osawa, M. Tsushima, H. Mogami, G. Samjeské, A. Yamakata, Structure of water at the electrified platinum-water interface: a study by surface-enhanced infrared absorption spectroscopy, J. Phys. Chem. C 112 (2008) 4248–4256.